Defect turbulence in a spiral wave pattern in the torsional Couette flow

A. Cros and P. Le Gal
Institut de Recherche sur les Phénomènes Hors Equilibre, UMR 6594, CNRS, and Universités d'Aix-Marseille I et II, 49 rue F. Joliot-Curie, BP 146, Technopôle de Château-Gombert, 13384 Marseille Cédex 13, France
(Received 2 March 2004; published 28 July 2004)

Our experimental study is devoted to the transition to defect turbulence of a periodic spiral wave pattern occurring in the flow between a rotating and a stationary disk. As the rotation rate Ω of the disk is increased, the radial phase velocity of the waves changes its sign: The waves that propagate first outward on average, then become stationary and finally propagate inward. As they become stationary, the nucleation of topological defects breaks the periodicity of the pattern. For higher Ω, more and more defects are generated in the flow pattern. This article presents the statistical study of this defect mediated turbulence.

DOI: 10.1103/PhysRevE.70.016309 PACS number(s): 47.20.Ft, 47.27.Cn, 47.54.+r

I. INTRODUCTION

One known scenario of transition to turbulence in extended systems is related to the nucleation of defects in periodic patterns [1,2]. This is the case for instance in Rayleigh–Bénard convection [3], in binary mixture convection [4], in Taylor–Dean system [5], or in electroconvecting nematics [6]. Topological defects in wave patterns have also been identified numerically in coupled amplitude equations [7], and a particular type of hole have even been found in the complex Ginzburg–Landau equation (CGLE) [8]. The mechanism of the transition from phase to defect chaos has been studied by Coullet *et al.*[9], who concluded that a topological defect was created by a diverging phase gradient. Brusch *et al.*[10] found that periodic coherent structures of the CGLE, called modulated amplitude waves (MAWs), evolved toward defects, as the period of these MAWs reached a critical minimum value.

We present in this article a study of the flow between a rotating and a stationary disk, a configuration which is of great interest from a fundamental point of view but also has many applications in turbomachines for instance. Moreover, rotating disk flows are often considered as model flows for the study of general three-dimensional flow instabilities. Our results may then be interesting for the understanding and the control of the transition to turbulence in boundary layers, pipe flows, or mixing layers for instance. In our experimental work, topological defects appear in a periodical wave (or roll) pattern appearing in the flow between a rotating and a stationary disk, through the local disappearance of a roll, or through the connection of two systems of rolls of different orientations. As the disk rotation rate Ω is increased, the number of these defects increases, and above a certain secondary threshold Ω_{TS} equal to 45 rpm (revolutions per minute) in the present configuration, spatially localized chaotic regions develop in the form of turbulent spirals (TSs) [11]. The defects are associated with strong amplitude modulations of the background waves and thus act as seeds for the birth of these TSs. We describe in this paper the appearance of the disorder in the periodical wave pattern, i.e., the transition to defect turbulence, until the first TSs appear.

II. EXPERIMENTAL APPARATUS AND DESCRIPTION OF THE FLOW

Our experimental device is the same as the one of Schouveiler, Le Gal and Chauve [12]. The rotating stainless-steel disk is immersed in a water-filled tank. Its drive shaft passes through the bottom of the tank and is connected to an electric motor through a belt. The rotation rate Ω of the disk is the control parameter of the experiment and can be varied from 0 to 200 rpm. The top lid of the container is the stationary disk. The radius of the disks is $R=14$ cm, and the distance h between the disks is set for these experiments to 2.1 ± 0.02 mm (except for some visualizations where a best contrast was obtained for other very close values of h). For this small h, and the considered rotation rate Ω, the shear is nearly constant in the fluid thickness [12] and this is the reason why this flow is called the torsional Couette flow. In order to visualize the flow patterns, water is seeded with reflective anisotropic flakes (Kalliroscope) whose orientation depends upon the local shear stress inside the flow. As the surface of the rotating disk is painted in black while the top one is a plexiglass plate, the flow pattern that develops between the two disks can be illuminated by a circular neon. A slight illumination inhomogeneity due to the neon tube electrical connections is barely visible but it will be any way, filtered out by image processing. Images are captured with a charge coupled device (CCD) camera placed 25 cm above this lid. This video camera is connected to a computer, and spatiotemporal diagrams can be performed in real time. These diagrams are performed along a radius, with a 25 Hz or 50 Hz sampling rate that gives between 30 and 60 images per disk revolution. They have a total duration of 4096 points in time and 512 points in space. In the following, we will use the disk rotation period as the time unit, while for figures describing an evolution in function of Ω, a second horizontal scale based on the Reynolds number ($\mathrm{Re}=\Omega R^2/\nu$, where ν is water viscosity) will also be presented.

Figure 1 shows an image of the whole disk when the periodical waves appear and the corresponding periodic space–time diagram. These spiral rolls were called "SRIII" by Schouveiler *et al.* and were also observed by San'kov and Smirnov [13] and Sirivat [14]. Their stability analysis was also analytically performed by Sank'ov and Smirnov [15]

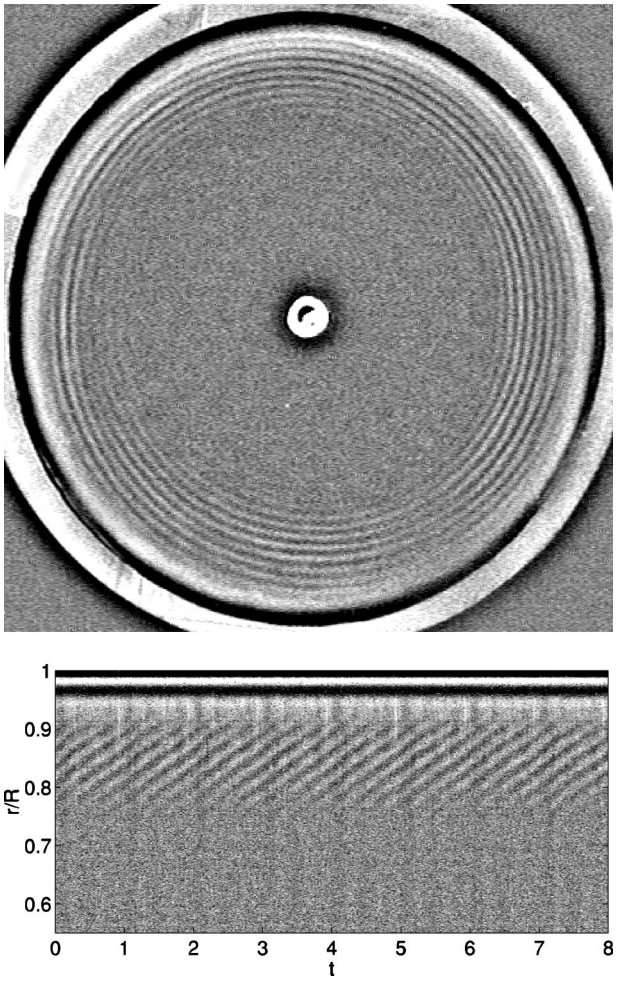

FIG. 1. SRIII for $h=2$ mm and $\Omega=38$ rpm clockwise ($\mathrm{Re}=7.8\times10^4$) (a). Corresponding space–time diagram where a perfect periodicity is observed closed to threshold (b).

who found a critical Reynolds number Re_h, based on the thickness of the fluid layer between 10 an 20. They also confirmed that the angle of the spirals versus the azimuthal direction is weak (between −5° and 4°) so that Chauve and Tavera [16] described them as nearly circular waves. Because of the weak value of this spiral angle, they are thought to be type II waves which are created by the combined effects of viscous and Coriolis forces [17]. Note also that Hoffmann *et al.* [18] calculated "stationary rolls" solutions in the Ekman Couette layer, corresponding to the SR III waves of our system. Indeed, as it will be seen in this work, their radial phase velocity can decrease to zero for some values of the control parameter Ω.

For $h=2.1$ mm, the spatiotemporal diagram recorded at threshold is presented in Fig. 2(a). The radial wavelength λ of the spirals as well as their temporal pulsation are well defined: The waves propagate toward the periphery of the disk with a constant velocity v_ϕ. When increasing Ω, an oscillation appears in the dynamical behavior of the spiral waves as shown in Fig. 2(b). This oscillation is in fact a precursor of an increasing disorganization observed for higher values of Ω and is, as can be seen in Fig. 2(b), synchronized on the disk rotation rate. Figure 2(c) shows the spatiotemporal diagram for $\Omega=40.5$ rpm. It can be observed that the waves possess now, on average, a very slight velocity toward the center of the disks: v_ϕ is weakly negative and has thus changed its sign. Moreover, some rolls are found to disappear at certain locations and at a certain time (see, for example, $t\simeq0.8$, $r/R\simeq0.82$), while some others appear at different places ($t\simeq2, r/R\simeq0.87$). For $t=1$, the signal presents a discontinuity for a whole interval in r/R, which reflects the passage on the acquisition line of a grain boundary between two systems of rolls of different orientations. Images of such defects are presented, respectively, in Figs. 3(a) and 3(b).

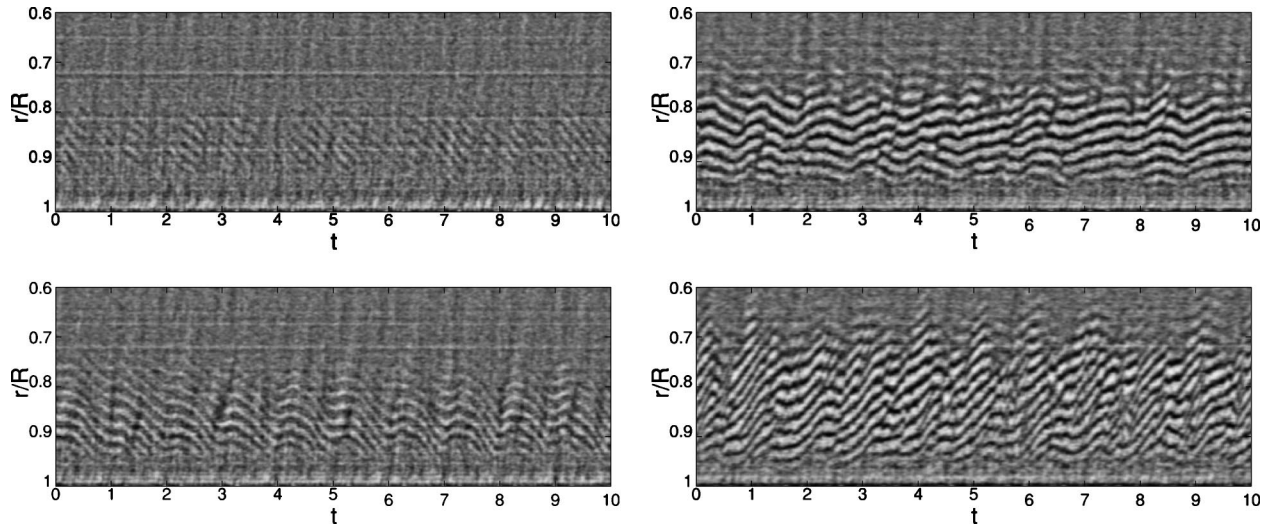

FIG. 2. Spatiotemporal diagrams for $h=2.1$ mm and (a) $\Omega=34.5$ rpm ($\mathrm{Re}=7.08\times10^4$), (b) $\Omega=36.5$ rpm ($\mathrm{Re}=7.49\times10^4$), (c) $\Omega=40.5$ rpm ($\mathrm{Re}=8.31\times10^4$), and (d) $\Omega=46$ rpm ($\mathrm{Re}=9.44\times10^4$).

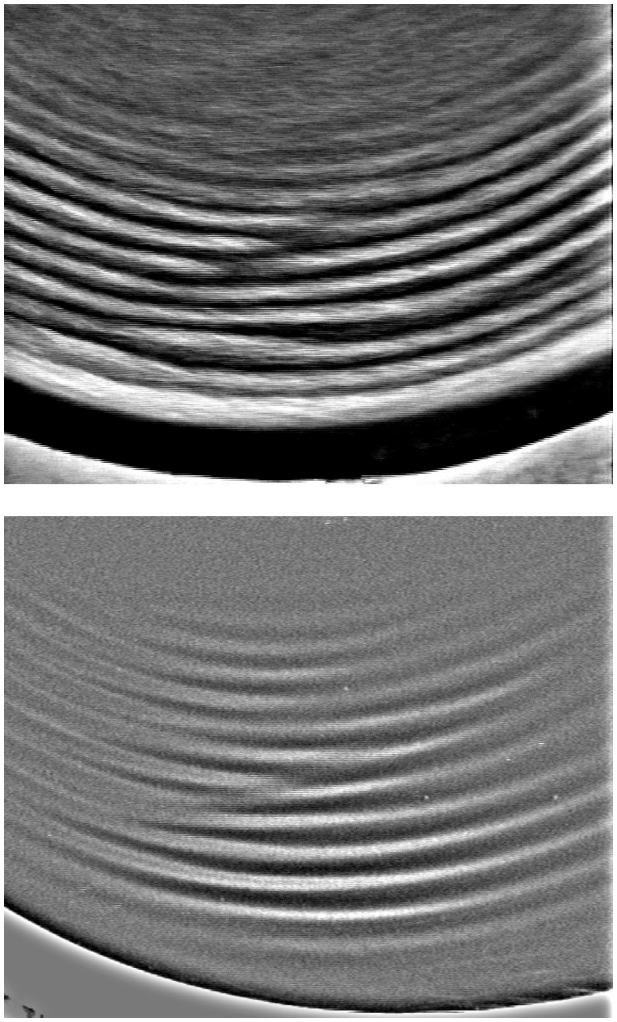

FIG. 3. a) Defect for $h=2$ mm and $\Omega=45$ rpm, b) defect for $h=2.1$ mm and $\Omega=43$ rpm. Clockwise rotation.

The first one is a dislocation [Fig. 3(a)]: The circulation of the phase of the periodic pattern around the defect is different from zero. Figure 3(b) presents a grain boundary: The rolls on the right-hand side of the image possess a higher inclination angle. For higher rotation rates, new structures appear in the flow: These are chaotic domains that we call TSs and show in Fig. 4. They appear on the large amplitude modulations associated with topological defects of the SR III pattern which act indeed as seeds for these turbulent spirals. Note that these TSs are similar to the turbulent helix (and not a spiral) of the cylindrical Couette flow or the turbulent band of the plane Couette flow [11]. Figure 4(b) shows a close-up of the flow at the turbulent spiral threshold. As it is observed, the underlying SR III pattern is strongly modulated and breaks up to let a turbulent domain take place in the flow. Above $\Omega_{TS}=45$ rpm, a transition to turbulence via a scenario of spatiotemporal intermittency has been described [11].

From the spatiotemporal diagrams, we can measure the characteristics of the spiral waves. Whereas the wavelength of the SR III keeps a constant value which is equal to twice the thickness h of the fluid layer, the radial phase velocity v_ϕ, as seen before, is found positive for values of Ω less than

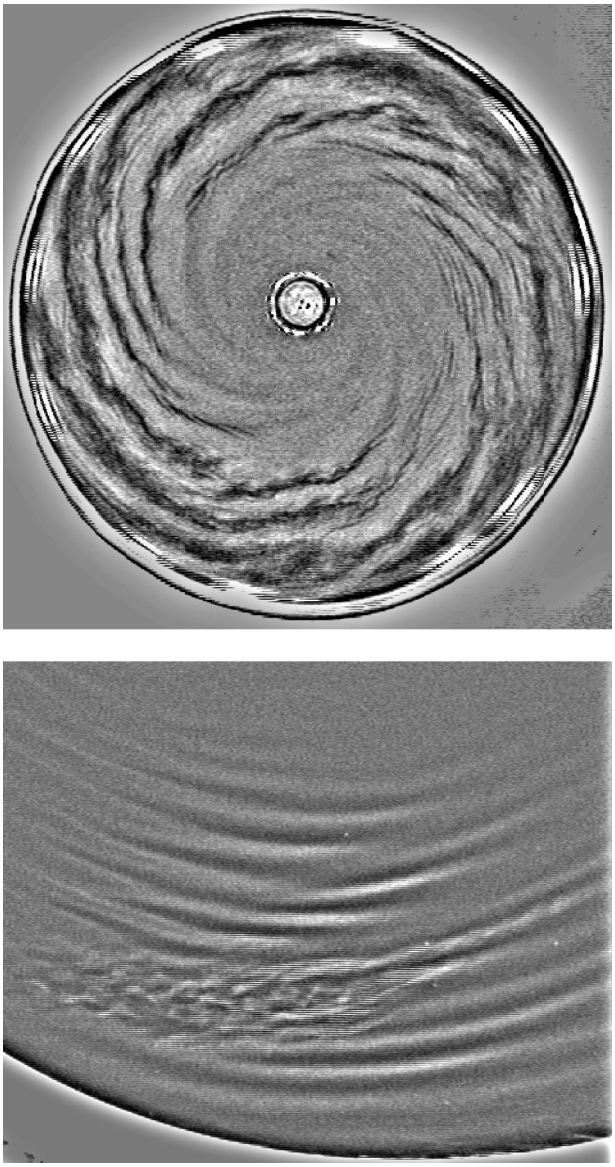

FIG. 4. (a) TSs for $h=1.8$ mm and $\Omega=74$ rpm clockwise (Re $=15.2\times10^4$). (Note that in Ref. [11], the images have been published reversed.) Close-up of a seed of a TS for $h=2.1$ mm and $\Omega=45$ rpm. Clockwise rotation.

40 rpm, and negative above this value. Figure 5 shows the evolution of v_ϕ. This is in accordance with the results of Hoffmann *et al.* [18] who calculated a vanishing phase velocity for the same kind of waves. Note also the linear evolution of v_ϕ with Ω.

III. TRANSITION TO DEFECT TURBULENCE

A. Evolution of the total number of defects

In order to automatically count the number of defects occurring in the flow pattern, a numerical procedure has been developed. It is based on the calculation of the Hilbert transform associated with space–time diagrams. As done in Refs. [19] or [20] the envelope of the wave pattern is computed. Figure 6(b) presents the spatiotemporal evolution of the en-

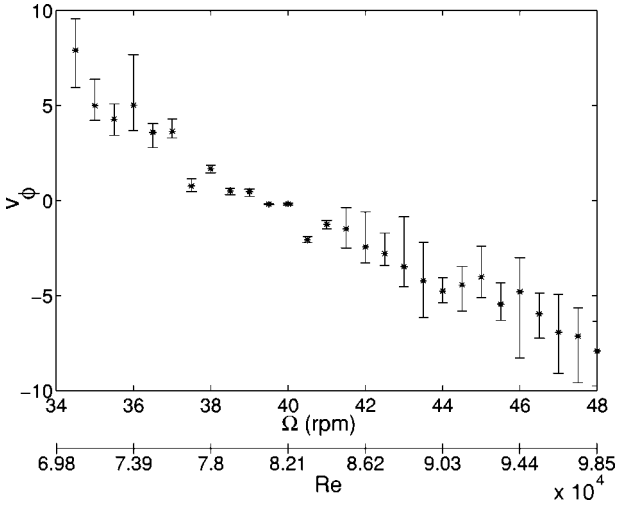

FIG. 5. Radial phase velocity v_ϕ as a function of Ω. $v_\phi > 0$ for an outward propagation, and $v_\phi < 0$ when the waves propagate toward the center.

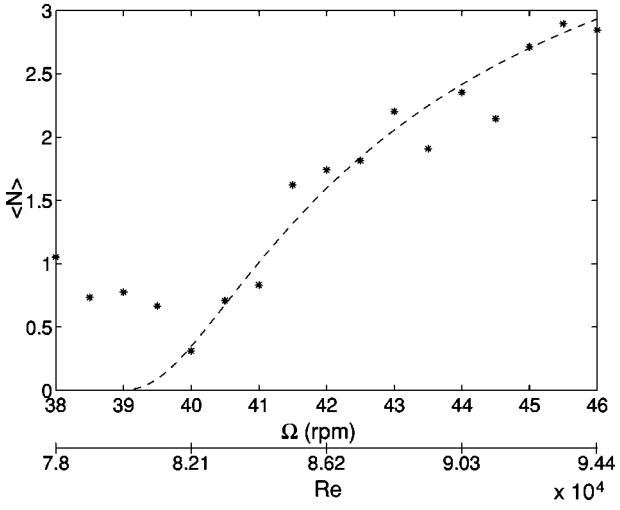

FIG. 7. Evolution with Ω of the mean number of defects per disk rotation. The dotted line is the curve predicted by Ref. [22] with $\alpha=1$, $a=5$, $b=4$, $c_3=\Omega$, and $c_3''=38.5$ rpm.

velope of the pattern presented in Fig. 6(a). As can be checked in Fig. 6(a), the dark regions correspond to depressions in the amplitude of the waves and are clearly associated with defects. The amplitude of the SR III waves being nearly zero in the core of the defects, a simple binarization process (using an adequate threshold) leads to the black and white pattern presented in Fig. 6(c). It is then quite obvious to count the total number of defects (independently of their durations) encountered on average per disk rotation on a region extended between $r/R=0.83$ and $r/R=0.9$, where the contrast of the images is high enough and the waves clearly observed. To insure the statistical convergence of this mean defect number, we have checked that the time durations of the analysis windows were long enough. Figure 7 presents the evolution of this mean number of defects per disk rotation. For Ω less than 40 rpm, the average number of defects is below 1 per disk rotation period. These defects are generated by the natural noise present in the SR III pattern close to its threshold. For values above $\Omega_c=40$ rpm, this number increases to 3. A transition occurs around $\Omega_c=40$ rpm, which is the value where the radial phase velocity changes its sign.

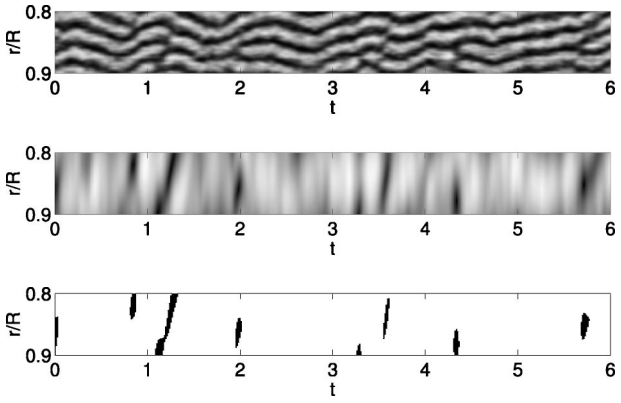

FIG. 6. Close-up of a spatiotemporal diagram for $h=2.1$ mm and $\Omega=40.5$ rpm, (b) envelope of the signal calculated by Hilbert transform of signal (a), and (c) binarization of envelope signal (b).

The absolute or convective nature of the SR III instability may be of some relevance to understand this feature. As the transition experienced by our hydrodynamical system shares similarities with the transition between phase turbulence and amplitude turbulence observed in the simulations of the Ginzburg–Landau equation [21], we plot together with our experimental data, a relationship similar to the one predicted in [22] using the facts that topological defects appear when the phase gradients have Gaussian fluctuations and diverge. The five coefficients in expression:

$$\langle N \rangle = a \exp\left(\frac{-b}{(c_3 - c_3'')^\alpha}\right), \tag{1}$$

are simply adjusted to fit our experimental data. The values $\alpha=1$, $a=5$, $b=4$, $c_3=\Omega$ and $c_3''=38.5$ rpm, give the best result and the smooth transition of an Arrhenius type can be observed in Fig. 7 [23], with an inflection point around $\Omega_c=40$ rpm.

B. Time distribution of defect occurrence

Another interesting interpretation of the transition to defect turbulence was performed by Afraimovich and Bunimovich in Ref. 24 and in the same spirit by Argentina, *et al.* [25]. The former consider a simple nonlinear version of a diffusion equation and show that a defect can be considered as a homoclinic orbit around a saddle-node critical point. Therefore, the time between defects corresponds to the length of the trajectories that leave and then come back in the vicinity of the fixed point. This duration τ_{lam} is thus controlled by the Liapunov exponent of the instability around the fixed point which possesses a logarithmic divergence at transition. Figure 8 presents the evolution with Ω of the mean lifetime τ_{def} of a defect and τ_{lam}, the time separating two consecutive defects. Contrary to τ_{def} which is nearly constant and equal to 0.1 disk rotation period, τ_{lam} shows a strong evolution with Ω. Before the transition, this average time is close to 1.5 disk rotation but climbs up to three rota-

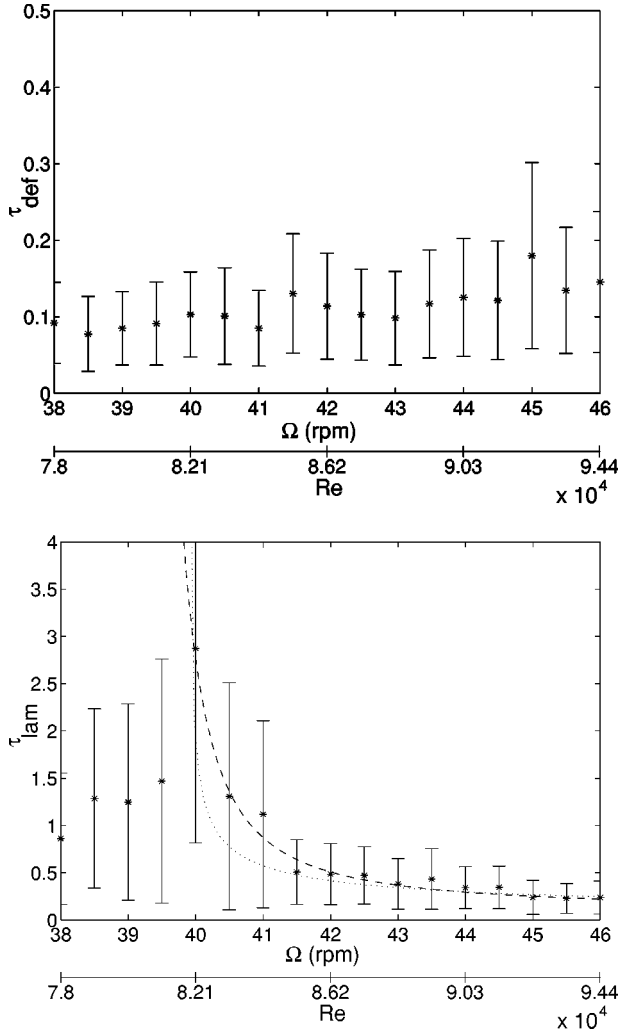

FIG. 8. Evolution of the mean lifetime τ_{def} of one defect (a) and of the time τ_{lam} separating two successive defects (b). The error bars represent the standard deviation of the statistics. The dashed line is a fit from relation (1) and the dotted line is the logarithmic divergence as calculated in Ref. [24].

tion periods for the critical value $\Omega=\Omega_c$ before it decreases back toward zero for higher values of Ω. Superimposed on the experimental data points, we show also the expected curves corresponding to defect number evolution given by Eq. (1) and also the logarithmic divergence similar to the one calculated in Ref. 24. As it can be seen, both evolutions are compatible with our data. Note, moreover, that the error bars given in Fig. 8 represent the standard deviations of the statistics of these typical times. Thus, a strong increase of the intensity of the fluctuations of τ_{lam} is observed near the defect turbulence threshold.

The complete statistics of the distribution of τ_{lam} versus Ω has also been calculated. Some examples are presented in Fig. 9 for four values Ω, where the cumulated histograms of τ_{lam}, that is the number N of occurrence of durations τ_{lam} larger than a given time T_{lam}. These semilogarithmic plots show that these distributions are exponential and a best linear fit of the experimental data leads to the determination of the slopes $-\lambda$ of these histograms.

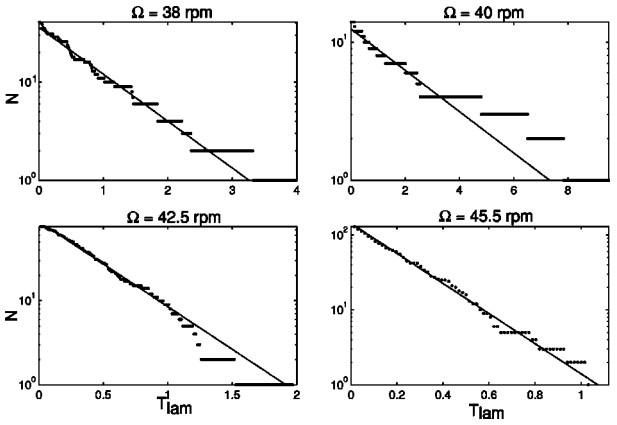

FIG. 9. Semilogarithmic plot of the cumulated histograms of the duration τ_{lam} for several values of the rotation rate Ω. Linear fits are also plotted.

Figure 10 shows the evolution of λ versus the average number $\langle N\rangle$ of defects when the disk rotation rate is varied. By definition, a Poisson distribution for the occurrence of defects in time is expected from the previous exponential shapes given in Fig. 9. In this case, the temporal duration of each defect is supposed to be zero and thus the evolution of λ versus Ω would be a line with a slope equal to 1. In Fig. 10(a), we can observe a slight deviation from this linear behavior. λ, which is the inverse of a characteristic time, is larger than the expected value. Therefore, the duration used to calculate the average number of defects $\langle N\rangle$ should be reduced. By simply subtracting from the total measuring time, the cumulated duration of defects, it is possible to correct the calculation of $\langle N\rangle$ by taking into account the average duration of a defect as presented in Fig. 8(a). This corrected defect number $\langle N^1\rangle$ is equal to $\langle N\rangle/1-\tau_{\mathrm{def}}$. Figure 10(b) presents the new evolution of λ which is closer to the expected behavior is recovered. This may indicate that the nucleation of a defect freezes the dynamics of the pattern around the defect and in a way validates the role of a homoclinic orbit as in the transition scenario of Ref. 24.

Therefore, it appears that if the distribution of occurrence of defects is quite well represented by a Poisson law near the transition threshold, it is necessary to take into account the effective duration of the defects as their density increases. This behavior is confirmed by the direct computations of the probability distribution $P(N)$ of defects when increasing Ω.

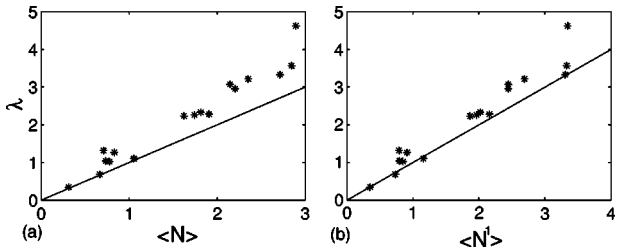

FIG. 10. Evolution of the slopes of the cumulated histograms as a function of the mean number of defects $\langle N\rangle$ (a), and as a function of the corrected mean number of defects $\langle N^1\rangle=\langle N\rangle/1-\tau_{\mathrm{def}}$ (b). The solid lines represent the expected behavior of the Poisson statistics.

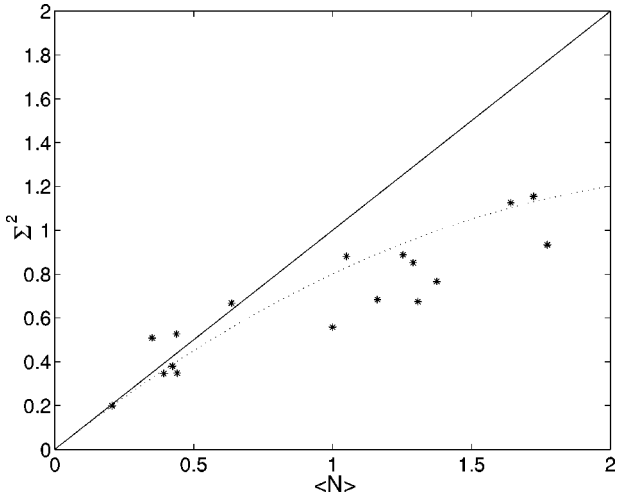

FIG. 11. Standard deviation of the defect distribution σ^2 as a function of the mean number of defects $\langle N \rangle$. The solid line would be the Poisson law characteristic and the dotted line is given by the binomial distribution.

C. Probability distribution of defect occurrence

As can be seen in Fig. 12, the experimental measurement of $P(N)$ shares some features with the expected general behavior of a Poisson distribution: Moreover, it can been checked in Fig. 11 that for the smallest values of Ω, the standard deviation increases quite proportionally to the mean. However, if we try to fit the Poisson law on the data, misfits appear starting at $\Omega = 42$ rpm. We then try to fit our data with the square Poisson law. Indeed, as shown in Ref. [26], in close systems, topological defects appear by pairs, inducing a modification of their probability distribution. But

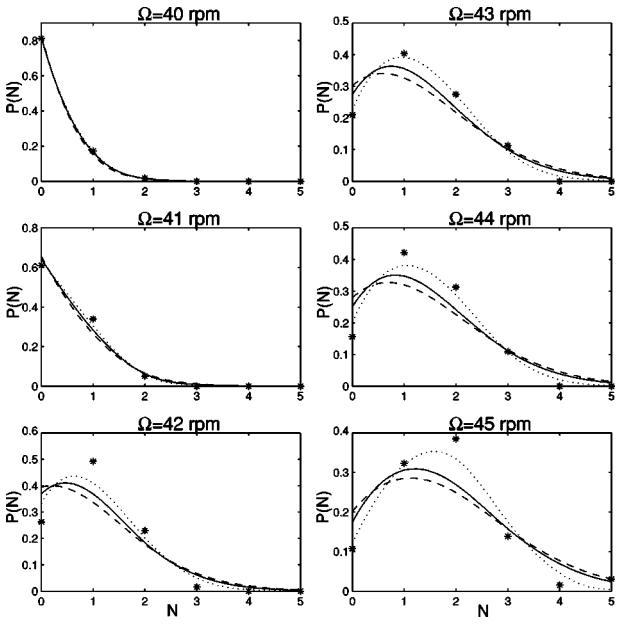

FIG. 12. Distribution of probability $P(N)$ of defect number per rotation for several rotation rate Ω. (*) experiments, Poisson law distribution (solid line), squared Poisson law distribution (dashed line), and binomial distribution (dotted line).

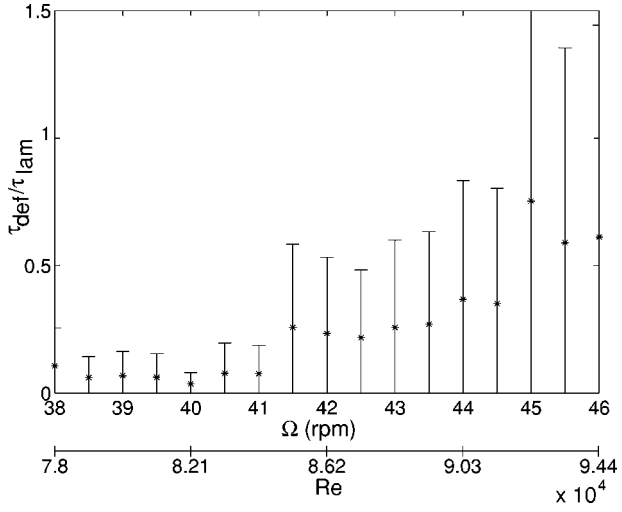

FIG. 13. Ratio $\tau_{\mathrm{def}}/\tau_{\mathrm{lam}}$ versus Ω. The error bars represent the standard deviation of the fluctuations. It can be observed that the ratio is larger than 1 for $\Omega \simeq \Omega_{\mathrm{TS}} = 45$ rpm.

it can be seen in Fig. 12 that the disagreement is worse. This is in fact not surprising as our system is not close: single defects can appear or disappear at the frontier of the SR III pattern. However, as we saw in the previous section, the time duration of each defect cannot be neglected as soon as the density of defects increases. Indeed, we are able to fit the experimental data by the binomial distribution of events, by adjusting the mean of this theoretical distribution with the experimental mean. The elementary probability p of the binomial distribution was then checked to be equal to the experimental probability $\pi_{\mathrm{def}}/\pi_{\mathrm{def}} + \tau_{\mathrm{lam}}$ to observe a defect.

D. Generation of turbulent spirals

The transition to a more developed turbulence occurs when the correlation length of the system becomes of the same order of the mean distance between defects [9]. Following the same idea, Afraimovich and Bunimovich [24] calculated a limit value of the defect density when $\tau_{\mathrm{def}} \simeq \tau_{\mathrm{lam}}$. With this aim, we calculate the ratio between τ_{def} and τ_{lam}. As can be seen in Fig. 13, this ratio first slightly decreases under the critical threshold to defect turbulence ($\Omega_c = 40$ rpm) and then progressively increases. As before, the error bars represent the standard deviations of the experimental data. For Ω larger than $\Omega_{TS} = 45$ rpm, we see that some values of the ratio $\tau_{\mathrm{def}}/\tau_{\mathrm{lam}}$ can be larger than 1: The distance between two defects is smaller than their own size. Moreover, these values of Ω around 45 rpm correspond to the apparition of the TSs studied in Ref. [11]. This confirms the role of the SR III pattern and its transition to defect turbulence, in the generation of the TSs of the torsional Couette flow.

IV. CONCLUSION

This study was devoted to the statistical description of an experimental observation of a transition toward defect turbulence in the wave patterns that appear in the gap flow be-

tween a rotating and a stationary disk. Using Hilbert transforms of space–time diagrams, an automatic counting of the increasing number of defects permits the characterization of the transition to defect mediated turbulence. This transition arises as the waves become stationary. Comparisons with models are quite satisfactory and show that the statistics of defect occurrence are well represented near the transition threshold by a Poisson process: Defects nucleate independently and their lifetime is small compared to the distance (in time or in space) that separates them. But as soon as their density is too large, that is when their lifetime is no longer negligible in front of their separating time, a binomial distribution of the defect occurrence gives a better fit of the experimental data. Finally, as the defect density increases, some strong amplitude modulations of the waves are generated: These will become seeds for the birth of localized TSs which are known to be highly nonlinear structures of the torsional Couette flow. Similar trends relative to the transition toward turbulence might then be searched in other open flows such as the plane or the cylindrical Couette flows, pipe flows, or boundary layers.

[1] M. Cross and P. C. Hohenberg, Rev. Mod. Phys. **65**, 851 (1993).

[2] D. Walgraef, *Spatio-Temporal Pattern Formation* (Springer, New York, 1997)

[3] A. Pocheau, V. Croquette, and P. Le Gal, Phys. Rev. Lett. **55**, 1094 (1985).

[4] A. La Porta and C. M. Surko, Phys. Rev. Lett. **77**, 2678 (1996).

[5] P. Bot and I. Mutabazi, Eur. Phys. J. B **13**, 141 (2000).

[6] E. Braun, S. Rasenat, and V. Steinberg, Europhys. Lett. **15**, 597 (1991).

[7] P. Coullet, C. Elphick, L. Gil, and J. Lega, Phys. Rev. Lett. **59**, 884 (1987).

[8] M. van Hecke, Phys. Rev. Lett. **80**, 1896 (1998).

[9] P. Coullet, L. Gil, and J. Lega, Phys. Rev. Lett. **62**, 1619 (1989).

[10] L. Brusch, M. G. Zimmermann, M. van Hecke, M. Bär, and A. Torcini, Phys. Rev. Lett. **85**, 86 (2000).

[11] A. Cros and P. Le Gal, Phys. Fluids **14**, 11, 3755 (2002).

[12] L. Schouveiler, P. Le Gal, and M. P. Chauve, J. Fluid Mech. **443**, 329 (2001).

[13] P. I. San'kov and E. M. Smirnov, Izv. Akad. Nauk SSSR, Mekh. Zhidk. Gaza **5**, 28 (1984); Fluid Dyn. **19**, 695 (1985).

[14] A. Sirivat, Phys. Fluids A **3**, 2664 (1991).

[15] P. I. San'kov and E. M. Smirnov, Izv. Akad. Nauk SSSR, Mekh. Zhidk. Gaza **6**, 79 (1991); Fluid Dyn. **26**, 857 (1991).

[16] M. P. Chauve and G. Tavera, in *Cellular Structures in Instabilities*, Lecture Notes in Physics Vol. 210, edited J. E. Weisfreid and S. Zaleski (Springer, Berlin, 1984), p. 307.

[17] D. K. Lilly, J. Atmos. Sci. **23**, 481 (1966).

[18] N. P. Hoffmann, F. H. Busse, and W. L. Chen, J. Fluid Mech. **366**, 311 (1998).

[19] V. Croquette and H. Williams, Physica D **37**, 300 (1989).

[20] P. Le Gal, Phys. Fluids A **4**, 2523 (1992).

[21] B. Shraiman, A. Pumir, W. Van Saarloos, P. Hohenberg, H. Chaté, and M. Holen, Physica D **57**, 241 (1992).

[22] D. A. Egolf and H. S. Greenside, Phys. Rev. Lett. **74**, 1751 (1995).

[23] C. Perez-Garcia, P. Cerisier, and R. Occelli, in *Propagation in Systems Far from Equilibrium*, edited by J. E. Wesfreid *et al.* (Springer, Berlin, 1988), p. 232.

[24] V. S. Afraimovich and L. A. Bunimovich, Physica D **80**, 277 (1995).

[25] M. Argentina, P. Coullet, and E. Risler, Phys. Rev. Lett. **86**, 807 (2001).

[26] L. Gil, J. Lega, and J. L. Meunier, Phys. Rev. A **42**, 1138 (1990).